Nuclear Physics A384 (1982) 65–87

FOLDING MODEL ANALYSIS OF α-PARTICLE ELASTIC SCATTERING WITH A SEMIREALISTIC DENSITY-DEPENDENT EFFECTIVE INTERACTION

A.M. KOBOS*

Nuclear Physics Laboratory, Oxford, UK and Max-Planck Institute fur Kernphysik, Heidelberg, Germany

B.A. BROWN and P.E. HODGSON

Nuclear Physics Laboratory, Oxford, UK

G.R. SATCHLER**

Oak Ridge National Laboratory, Oak Ridge, Tennessee 37830, USA

and

A. BUDZANOWSKI

Institute of Nuclear Physics, 31-342 Cracow, Poland

Received 18 January 1982

Abstract: Differential cross sections for the elastic scattering of α-particles from ^{40}Ca, ^{46,48,50}Ti, ^{58}Ni, ^{90}Zr and ^{208}Pb at 140 MeV and from ^{58,60,62,64}Ni at 172 MeV are analysed using a double-folding model with a semirealistic density-dependent effective interaction based on the M3Y interaction for the real potential and various phenomenological imaginary potentials. Very good fits with consistent parameters of the model have been obtained.

The application of the folding model analyses of α-particle elastic scattering to the determination of the nuclear matter density distribution is critically examined.

1. Introduction

The elastic scattering of α-particles at energies high enough for the refractive rainbow scattering at angles larger than the rainbow angle to be observed resolves the discrete ambiguities of the optical potential that occur in analyses of data at lower energies. The value of the rainbow angle and the slope of the differential cross section beyond it essentially depend on the real potential and so its depth can be uniquely determined. In this way Goldberg [1]) established the superiority of real potentials with Woods–Saxon squared form factors and depths around 140 MeV.

Another advantage of analysing the data at higher energies is that since no potential pocket exists for the grazing l-values, the cross section is almost exclusively

* On leave from Institute of Nuclear Physics, Cracow, Poland.

** Research sponsored by the Division of Basic Energy Sciences, US Dept. of Energy.

due to the barrier scattering amplitudes with no interference from the internal wave amplitudes [2]). This leads to a reduced sensitivity of the cross section to the details of the complex potential. For these reasons the elastic scattering of α-particles at high energies, probing further into the target nucleus, can be used to assess the applicability of different folding models to calculate the real potential.

Folding model potentials can be calculated in two ways:

(a) The single folding model uses a parametrized α-nucleon interaction folded with the target density or a nucleon–target optical potential folded with the α-particle density. This latter potential does not include properly the density dependence of the interaction or its surface features or the couplings to other channels as discussed by Satchler and Love [3]). These effects lead to a considerable overestimate of the strength of the real potential, and indeed Goldberg [4]) showed that a single-folded potential is much too deep to fit the rainbow scattering.

(b) The double-folded model expresses the potential in terms of an effective nucleon–nucleon (NN) interaction between the nucleons of the interacting nuclei integrated over both their densities. The effective interaction calculated in the medium of the two nuclei can remove some of the shortcomings of the effective interactions used in the single-folding approach. However, the depth of the double-folded potential for α particles is still overestimated, and in a realistic analysis it proved necessary to explicitly include the antisymmetrization-exchange effects and the density-dependent saturation effects in the effective NN interaction [5]).

Essentially, the density dependence of the effective interaction arises from the Pauli principle effects in the overlapping region and from the energy denominator of the Bethe–Goldstone equation [6]).

The aim of this work was to study more precisely the density dependent effective interaction applied in the double-folding model and to examine the extent to which folding model analyses of α-particle elastic scattering can be used to determine nuclear matter densities, particularly in the view of their crucial importance when the effective interaction is explicitly dependent upon the densities.

2. Definition of the potential and outline of the fitting procedure

The double folded real potential may be written [3])

$$U_{\mathrm{F}}(\boldsymbol{R}) = \int \mathrm{d}\boldsymbol{r}_1 \int \mathrm{d}\boldsymbol{r}_2\, \rho_1(\boldsymbol{r}_1)\rho_2(\boldsymbol{r}_2)t(\boldsymbol{s} = \boldsymbol{R} + \boldsymbol{r}_2 - \boldsymbol{r}_1)\,, \tag{1}$$

where $\rho_i(\boldsymbol{r}_i)$, $i = 1, 2$, are the density distributions of the point-like nucleons in the ground state of the ith (projectile and target) nuclei, $\boldsymbol{R}$ is the separation of the centres-of-mass of the colliding nuclei, and t is the effective NN interaction which may depend on the local densities ρ_1 and ρ_2 and on energy in ways to be discussed later.

For the elastic scattering of spinless particles the potential U_F is calculated using only the isoscalar $t_{S=0,T=0}$ component of the effective interaction since the isovector ($T=1$) term in the effective interaction does not contribute in this case.

In the analyses, the folded real potential was allowed an overall adjustable normalization λ. The imaginary potential was taken as a phenomenologically fitted Woods–Saxon, (WS), or Woods–Saxon-squared, $(WS)^2$, form.

Some attempts to use for the imaginary potential the same folded potential as the real one, except for a different normalization, did not prove successful [7]. Theoretical calculations of the imaginary potential by Vinh Mau [8] have not been used to fit experimental data.

The imaginary potential used in our analysis has one of the forms

$$W(r) = -W_V f_V(r)\,, \tag{2a}$$

$$W(r) = -W_V f_V^2(r)\,, \tag{2b}$$

$$W(r) = -W_V f_V^2(r) + 4a_D W_D \frac{\mathrm{d}f_D^2(r)}{\mathrm{d}r}\,, \tag{2c}$$

where

$$f_{V,D}(r) = \left[1+\exp\left(\frac{r-r_{V,D}A_T^{1/3}}{a_{V,D}}\right)\right]^{-1}. \tag{3}$$

Form (2c) is a mixture of volume and derivative (surface) terms with independent geometrical parameters (r_V, a_V) and (r_D, a_D).

The Coulomb potential $V_C(r)$ of a uniformly charged sphere of radius $R_C = 1.34A_T^{1/3}$ was used throughout the calculations.

The total scattering potential is then

$$V(r) = -\lambda U_F(r) + iW(r) + V_C(r)\,. \tag{4}$$

The analysis was performed using our comprehensive optical model code which utilizes the double folding (in momentum space) routines originally written by Cook [9] and modified to include a density-dependent effective interaction and shell-model densities as calculated by the Oxford Shell-Model Density code. The searches for three (or six) parameters of the imaginary potential and the overall normalization λ of the real folded potential U_F were made using the CERN minimizing program package MINUIT [10].

Applying the double folding procedure to the real potential with phenomenological WS or $(WS)^2$ imaginary potentials we have analysed the following data for high energy α-particle scattering:

(i) ^{58,60,62,64}Ni(α, α) at 172.5 MeV [Budzanowski *et al.* [11])],

(ii) ^{90}Zr(α, α) at 140 MeV; ^{40}Ca(α, α) at 141.7 MeV; ^{58}Ni(α, α) at 139 MeV) [Goldberg *et al.* [12])],

(iii) ^{208}Pb(α, α) at 140 MeV [Goldberg *et al.* [13])],

(iv) ^{46,48,50}Ti(α, α) at 140 MeV [Roberson *et al.* [14])].

Before presenting our final results we discuss in the next section the components of the calculation of the folded real potential (1) and also present some intermediate results.

3. The effective interaction

The effective interaction applied in the double-folding formula (1) is the M3Y interaction of Bertsch *et al.* [15]) based on the *G*-matrix elements of the Reid NN interaction, supplemented by a single-nucleon exchange term (SNE). In parametrized form it is: [3])

$$t_{00}(s, E) = 7999\frac{e^{-4s}}{4s} - 2134\frac{e^{-2.5s}}{2.5s} + \hat{J}_{00}(E)\,\delta(s)\,,$$

with

$$\hat{J}_{00}(E) = -276(1 - 0.005E_p/A_p)\,. \tag{5}$$

This interaction averaged at $E_p/A_p = 10\,\mathrm{MeV}/A_p$ has been widely and in general successfully used to analyse heavy ion elastic scattering [3]). We note that:

(i) This interaction is density independent. It is an average over some range of densities [3]), and is thought to be typical of an average density of perhaps $\frac{1}{3}$ of the density ρ_0 of normal nuclear matter.

(ii) The energy dependence of the M3Y interaction (5) is not important for heavy ions [3]), but this is not so for light projectiles at high energies [16]).

3.1. RESULTS WITH THE M3Y FOLDED REAL POTENTIAL

We first describe calculations made with density-independent interactions. With the interaction (5) and nuclear densities obtained as described in sect. 5 we calculated the M3Y double folded real potential (1) for the nuclei and energies listed above. As an example we discuss here the results for $\alpha + {}^{58}$Ni at 172.5 MeV obtained with a volume $(\mathrm{WS})^2$ imaginary potential (2b). The depth of the M3Y potential (with $\hat{J}_{00} = -216.5\,\mathrm{MeV}\cdot\mathrm{fm}^3$ was -231 MeV, and for a 'standard' value of $\hat{J}_{00} = -262\,\mathrm{MeV}\cdot\mathrm{fm}^3$, corresponding to $E = 10\,\mathrm{MeV}/A_p$, it was -264 MeV.

The M3Y potential produced a broad maximum in the cross section between 40° and 65° followed by a fall-off at larger angles. Renormalizing the M3Y potential by 0.55, we were only able to obtain a qualitative fit to the data ($\chi^2/F \approx 89$, F being the number of degrees of freedom) as shown in fig. 1 by curve labelled RM3Y (the potential RM3Y is given in table 8). It is not only the region of the rainbow angle but also the fine diffraction structure in the cross section at very forward angles that is very difficult to fit simultaneously with the rainbow scattering. Since the forward-angle scattering is most sensitive to the potential near the strong absorption radius, this means that with such a large renormalization, the renormalized M3Y potential is much too shallow in the nuclear surface.

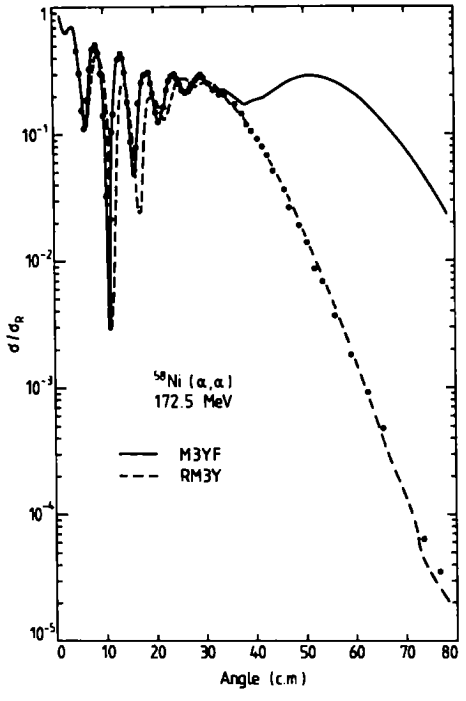

Fig. 1. The "best" fit to ^{58}Ni(α, α) at 172.5 MeV with the density-independent M3Y renormalized potential (RM3Y) and the one when the fitting procedure was restricted to forward angles <30° (M3YF).

We also fitted with the M3Y potential the data limited to the diffraction region up to $\theta = 30°$. With a little renormalization, 0.96 (the potential M3YF of table 8) we obtained a very good fit ($\chi^2/F = 3.0$) in this angular region shown by the curve M3YF in fig. 1. This fit is almost of the same quality as obtained with the density dependence described later (the corresponding $\chi^2/F = 2.5$) but is quite unacceptable beyond the rainbow angle. The potential in the first case above is 1.8 times deeper in the surface (at the strong absorption radius) than the previous largely renormalized M3Y potential, and it is close to the density-dependent potential in the second case.

The general features of the M3Y folded potential described here have persisted for all the cases studied.

This model calculation again shows the necessity of large-angle data in the rainbow region for an unambiguous determination of the real potential.

At this point we should like to comment that a successful application of the pure M3Y potential to $\alpha + ^{40}$Ca elastic scattering at 29 MeV [ref. [17])], resulting in a deep real folded potential of about 250 MeV, was probably untypical. Later model-independent analyses [18]), of the same experimental data resulted in potentials much shallower in the interior and this agrees well with our potentials to be described

in this paper, although obviously the model-independent analyses are inherently capable of giving better fits. Thus the real double folded M3Y potential is clearly too deep in the centre. One way to remedy this is to apply a density dependence to the effective interaction.

4. The density dependence

We first applied the density dependence of the G-matrix elements (so-called DDD interaction) of Eisen and Day [6]) in the same way as for heavy ions [3]). The effect was to decrease the central depth of the folded real potential by merely 5% with no effect on the calculated rainbow scattering which is inconsistent with experimental data. Fitting the data with the folded potential of this type gave very similar results to those previously described (subsect. 3.1) with the pure M3Y potential. This density dependence has little effect on α-particle scattering as was previously found for heavy ion scattering [3]).

In order to simplify the calculations, it was assumed that the density dependence and the radial dependence could be factorized as in [19])

$$t^E(s, \rho) = g^E(s) f^E(\rho), \tag{6}$$

where $g^E(s)$ is a function of the distance s, in our case given by the M3Y interaction (5), and $f^E(\rho)$ is a function of density, for given energy E.

A study of the energy and density dependence of the real isoscalar optical potential, based on the Brueckner–Hartree–Fock nuclear matter calculations of Jeukenne *et al.* [20]), provides a convenient way of introducing the density dependence into the folding calculations. The density dependence of their quantity $|V_0|/\rho$, which is the volume integral of the interaction per nucleon (for a given energy), can be easily parametrized with an exponential form:

$$f(\rho) = C_\rho(1 + \alpha\, \mathrm{e}^{-\beta\rho}), \tag{7}$$

with parameters C_ρ, α and β that may depend on energy. This form is rather similar to another parametrization of the density dependence $f(\rho) = C(1 - \alpha\rho^{2/3})$ introduced by Myers [21]). One of the possible prescriptions for the density entering (7) is that ρ is the density midway between the two interacting nucleons, but in the view of the short range of the effective interaction it is sufficiently accurate to use the more convenient form $\rho = \rho_1(r_1) + \rho_2(r_2)$ [refs. [22,3])]. This approximation has been studied by Goldfarb and Nagel [23]) and was found to underestimate the folded potential up to about 15% in the inner radial regions for $\alpha + {}^{40}$Ca at 29 MeV, i.e. when the projectile penetrates deeply into the target nucleus. Such an approximation allows easily for the factorization of the density-dependent interaction necessary to perform the folding calculation in momentum space, but it may lead to a non-realistic build up of the nuclear densities. We shall briefly discuss this point later in our conclusions. The density dependence (7) has been successfully used for

a heavy ion calculation [22]), with the parameters $\alpha = 6.2$ and $\beta = 8.64\ \mathrm{fm}^{-3}$ corresponding to $|V_0|/\rho$ of ref. [20]), calculated for $E_p/A_p = 10\ \mathrm{MeV}/A_p$.

So far, the constant C_ρ in (7) was treated somewhat arbitrarily. It has for instance been proposed [24]) that C_ρ should be determined by the requirement that $f(\rho) = 1$ for $\rho = \frac{1}{3}\rho_0$, with ρ_0 being the "normal" nuclear density, $\rho_0 = 0.17\ \mathrm{fm}^{-3}$. This means that for this particular density one would regain the M3Y interaction, in the agreement with the heavy ion scattering results already obtained with the M3Y interaction [3]). This normalization is based, for example, on the finding that the M3Y interaction has a strength similar to that of the density-dependent DDD interaction [6]), mentioned at the beginning of this section, at $\rho = \frac{1}{3}\rho_0$.

The data we have been analysing are for energies corresponding to E_p/A_p equal to 43 and 35 MeV/A. Due to a considerable energy dependence of the density dependence, that becomes weaker with increasing energy [20]), we adopted another approach.

In the nuclear matter calculations the volume integral of the G-matrix for one bound and one free nucleon interacting in the presence of nuclear matter of density ρ, with the assumption (6), is

$$\frac{V_0(\rho, E)}{\rho} = \int g^E(s) f^E(\rho)\, \mathrm{d}^3 s\,, \tag{8}$$

where $g^E(s)$ is the radial part of the effective interaction and $f^E(\rho)$ is its density dependence for a given energy. With $f^E(\rho)$ given by (7) we have

$$\frac{V_0(\rho, E)}{\rho} = C_\rho(E)(1 + \alpha(E)\, \mathrm{e}^{-\beta(E)\rho}) \int g^E(s)\, \mathrm{d}^3 s\,. \tag{9}$$

For the two energies studied, we calculated the normalizing constants C_ρ, having precisely fitted $|V_0|/\rho$ calculated according to ref. [20]) with the exponential form (7), and assuming the radial dependence $g^E(s)$ to be the same as the energy-dependent M3Y interaction (5) for $t(s, E)$. (We should note, however, that the calculations of ref. [20]) only extend to densities around that of normal nuclear matter, whereas larger densities are encountered in the folding calculation in the nuclear interior. In addition, the effects of density gradients are ignored.)

The effective interaction finally used in the folding formula (1) is then

$$-t(s, \rho) = \left(-7999\, \frac{\mathrm{e}^{-4s}}{4s} + 2134\, \frac{\mathrm{e}^{-2.5s}}{2.5s} - \hat{J}_{00}\, \delta(s)\right) C_\rho(1 + \alpha\, \mathrm{e}^{-\beta(\rho - \rho_1 + \rho_2)})\,. \tag{10}$$

We call this the density-dependent M3Y interaction (DDM3Y). The parameters and volume integrals of this interaction used for the two energies are given in table 1.

The normalizing constants C_ρ, as listed in table 1, in the density dependence (7) obtained by normalizing to the results of ref. [20]) correspond to $f(\rho) = 1$ for $\rho_1 + \rho_2 = 0.090\ \mathrm{fm}^{-3}$ at 172.5 MeV and to $0.095\ \mathrm{fm}^{-3}$ at 140 MeV. For these densities the volume integrals J_0 of the DDM3Y interaction are equal to the volume integrals

TABLE 1

The parameters and volume integrals J_0 of the M3Y and density-dependent M3Y (DDM3Y) interactions

E (MeV)	$\hat{f}_{00}$ (MeV · fm^3)	C_ρ	α	β (fm^3)	J_0 (M3Y) (MeV · fm^3)	$J_0(\rho=\frac{1}{2}\rho_0)$ (DDM3Y) (MeV · fm^3)	$J_0(\rho=\rho_0)$ (DDM3Y) (MeV · fm^3)
140	−227.7	0.279	5.141	7.202	373.3	460.2	261.6
172.5	−216.5	0.204	6.814	6.152	362.2	428.1	250.2

of the corresponding pure M3Y interaction. As can be seen from the volume integrals listed in table 1, the effect of the density dependence is to considerably reduce the interaction at large densities and to enhance it at small densities. As required this density dependence will have a larger effect than that of the DDD interaction. The effect at large densities does not depend on energy while at small densities it decreases with energy. Encouragingly the numbers of table 1 are reasonable and consistent for the two energies. Should we however want to incorporate the final overall normalization factor $\lambda \approx 1.3$ for the real potential, as obtained in this work, into $C'_\rho = \lambda C_\rho$ then the value of $\rho_1+\rho_2$ corresponding to $f(\rho)=1$ would be 0.14 fm^{-3}.

5. The nuclear densities

The nuclear matter distributions are calculated by summing the absolute squares of the wave functions of the occupied orbits, weighted by the occupation probabilities.

The potential has the form

$$V(r) = V_C(r) + Uf_1(r) + \left(\frac{\hbar}{m_\pi c}\right)^2 U_s \frac{1}{r}\frac{df_2(r)}{dr} \boldsymbol{L}\cdot\boldsymbol{\sigma}\,, \tag{11}$$

where $V_C(r)$ is the electrostatic potential due to a uniformly charged sphere of radius $R_C = r_C A^{1/3}$ and charge $Z-1$, U and U_s are potential depths, and the form factor $f_i(r) = [1+\exp\{(r-R_i)/a_i\}]^{-1}$ with $R_i = r_i A^{1/3}$.

The values of the parameters U, r_1 and a_1 of this potential were fixed to reproduce the experimental quantities for ^{40}Ca and ^{208}Pb listed in table 2. The values of the parameters for other nuclei were obtained using the interpolation and extrapolation formula

$$X(N,Z;\mathrm{p/n}) = X_0 \pm X_1\left(\frac{N-Z}{A}\right) + X_2(A^{1/3}-(208)^{1/3})\,. \tag{12}$$

The parameters for the spin-orbit potential were fixed to the values $U_s = 6$ MeV; $r_2 = 1.1$ fm, $a_2 = 0.65$ fm.

TABLE 2

Data fitted by the standard potential

Nucleus	E_p [a]) (MeV)	E_n [a]) (MeV)	r_{ch} (fm)	$r_p - r_n$ (fm)	$\tilde{a}_{ch}$ (fm)	$\tilde{a}_p - \tilde{a}_n$ (fm)
^{40}Ca	8.64		3.477		0.521	
^{208}Pb	8.17	7.79	5.514	−0.20 [b])	0.510	−0.10 [b])

[a]) E_p and E_n are the energies of the occupied orbits nearest the Fermi surface.
[b]) Estimates based on the result of Skyrme HF calculations and the tail densities of neutron orbits from heavy ion sub-Coulomb stripping experiments [25]).

In table 2, the diffuseness $\tilde{a}$ is defined in terms of the second and fourth moments of the distribution

$$\tilde{a} = \left[\frac{3(R_4 - R_2)(9R_2 - 7R_4)}{2\pi^2}\right]^{1/2}, \tag{13}$$

where

$$R_L = \left[\frac{L+3}{3}\frac{\int \rho(r) r^{L+2}\,\mathrm{d}\tau}{\int \rho(r) r^2\,\mathrm{d}\tau}\right]^{1/L}. \tag{14}$$

The energies E_p and E_n are those of the occupied proton or neutron state nearest the Fermi surface, and the radii quoted are all point radii except for the charge distribution.

With these parameters the wave functions of all single-particle states can be calculated, and hence the required density distributions from the expression

$$\rho(r) = \sum_i a_i |\psi_i|^2, \tag{15}$$

where a_i are occupation numbers and the sum runs over all occupied orbits.

For the closed shell nuclei ^{40}Ca, ^{90}Zr and ^{208}Pb the occupation numbers were set to those of the extreme single-particle shell model. For the Ni isotopes these were supplemented by shell-model calculations of the occupation numbers as given in table 3. For ^{40}Ca calculations were also made with the Hartree–Fock formalism

TABLE 3

Occupation numbers for the Ni isotopes as obtained by Koops [26])

	^{58}Ni		^{60}Ni		^{62}Ni		^{64}Ni	
	$\langle\pi\rangle$	$\langle\nu\rangle$	$\langle\pi\rangle$	$\langle\nu\rangle$	$\langle\pi\rangle$	$\langle\nu\rangle$	$\langle\pi\rangle$	$\langle\nu\rangle$
$1f_{7/2}$	8.00	8.00	8.00	8.00	8.00	8.00	8.00	8.00
$2p_{3/2}$	0	1.17	0	1.98	0	2.61		3.15
$1f_{5/2}$	0	0.64	0	1.54	0	2.53		3.55
$2p_{1/2}$	0	0.19	0	0.48	0	0.86		1.30

TABLE 4

Properties of the calculated densities

	Occupation numbers	Potential	$\langle r^2\rangle_{ch}^{1/2}$ (fm) exp	$\langle r^2\rangle_{ch}^{1/2}$ (fm) theor	$\tilde{a}_{ch}$ (fm) theor	$\langle r^2\rangle_n^{1/2}-\langle r^2\rangle_p^{1/2}$ (fm) theor	$\tilde{a}_m$ [c] (fm) theor
^{40}Ca	[a]	WS	3.483 (3) [d]	3.477	0.521	−0.089	0.481
		Skyrme 3		3.473	0.475	−0.036	0.437
^{46}Ti	[a]	WS	3.614 (4) [d]	3.576	0.506	−0.012	0.473
^{48}Ti	[a]	WS	3.599 (4) [d]	3.570	0.496	0.072	0.470
^{50}Ti	[a]	WS	3.576 (4) [d]	3.567	0.488	0.146	0.468
^{58}Ni	[b]	WS	3.777 (5) [e]	3.849	0.495	−0.047	0.469
	[a]	WS		3.848	0.495	−0.047	0.474
^{60}Ni	[b]	WS	3.815 (6) [e]	3.852	0.487	0.020	0.477
	[a]	WS		3.848	0.487	0.021	0.490
^{62}Ni	[b]	WS	3.844 (5) [e]	3.857	0.480	0.080	0.486
	[a]	WS		3.854	0.480	0.088	0.508
^{64}Ni	[b]	WS	3.862 (5) [e]	3.864	0.474	0.133	0.495
	[a]	WS		3.862	0.474	0.138	0.508
^{90}Zr	[a]	WS	4.263 (8) [f]	4.256	0.534	0.096	0.490
^{208}Pb	[a]	WS	5.503 (5) [g]	5.514	0.510	0.206	0.538

[a] Extreme single-particle model.
[b] See table 2.
[c] Diffuseness parameter as defined by eq. (13) for the point neutron plus proton matter distribution.
[d] Wohlfahrt *et al.* [29]).
[e] Wohlfahrt *et al.* [30]).
[f] Rothhaas [31]).
[g] Frois *et al.* [32]).

using the Skyrme 3 interaction [27,28]). Some properties of the calculated densities are summarized in table 4.

The theoretical rms charge radii obtained from the above methods are generally in agreement with experiment for all nuclei in the region $A = 40$–208 to within less than 1%. Since the experimental charge radii for most stable nuclei have been measured to an accuracy of about 0.1%, the theoretical densities were adjusted to give exactly the measured charge radii by scaling all densities by the monopole Werntz and Überall model [33]),

$$\rho'(r) = \rho(r) + \tfrac{1}{2}\left[1 - \frac{\langle r^2\rangle_{ch,exp}}{\langle r^2\rangle_{ch,th}}\right]\left(3\rho(r) + r\frac{d\rho(r)}{dr}\right), \tag{16}$$

which maintains the constancy of the nucleon number. This scaling has a negligible effect on $r_n - r_p$.

For the α-particle density we used the point proton matter density obtained by Sick [34]) from a model-independent analysis of the experimental α-charge form factor [35,36]) which takes into account the proton and neutron finite charge distribu-

tions. It is a good approximation to take $\rho_n(r) = \rho_p(r)$. We mention that the point density obtained by Sick [34]) is unusual in that there is a marked depression in the interior density (inside 0.7 fm) which cannot yet be understood theoretically. This depression may be due to mesonic exchange effects in the charge form factor [37]) which were not included in the analysis of Sick [34]), which would mean that the point nucleon density could actually be more normal in the interior. However, given that this effect is not important until large momentum transfer in the form factor ($q \approx 3\,\mathrm{fm}^{-1}$) and that the nucleon probability distribution involved in the central depression is small (because of the r^2 factor), this uncertainty will have little effect on the present results.

6. The results

We have analysed the experimental data listed in sect. 2 with the double folded density-dependent M3Y real potential with an overall normalization factor λ and three different types of imaginary potentials:

(i) Woods–Saxon volume potential [WS], cf. (2a);

(ii) Woods–Saxon-squared volume potential [$(WS)^2$], cf. (2b);

(iii) Woods–Saxon-squared volume plus Woods–Saxon surface (derivative) potentials with independent geometries [$(WS)^2 + D$], cf. (2c).

These three imaginary potentials constitute a phenomenological attempt to find how the cross-section depended on the shape of the imaginary potential. We did not try a model-independent (spline) parametrization of the imaginary potential since it appeared that we have given a sufficient flexibility to the imaginary potential by using type (2c) above.

The results of fitting are summarized in tables 5, 6 and 7. In fig. 2 we show the best fits for ^{58,60,62,64}Ni(α, α) at 172.5 MeV with imaginary potential (2c). We do not show the remaining fits since the data have been published elsewhere and our calculated cross sections essentially go through all the experimental points. In general the quality of fit is very good. We comment that for ^{60}Ni 25% of the total χ^2 comes from one data point at 46°. For ^{62}Ni 84% of the total χ^2 comes from a single point near the minimum at 10.5°, and without this point χ^2/F would be 1.05. We believe that the experimental angular resolution may be extremely important for points in this very deep and sharp minimum. For ^{58,60,62,64}Ni(α, α) at 172.5 MeV we also fitted the data with a phenomenological $(WS)^2$ real and $(WS)^2$ imaginary potentials, and the corresponding χ^2/F, volume integrals and rms radii are given in parentheses in table 5. It seems that we can approach with the folded real potential the limits in fitting achieved with the phenomenologically fitted real $(WS)^2$ potential. Moreover, for many cases we are close to the limits set by model-independent analysis [38]).

The fits obtained for ^{46,48,50}Ti(α, α) at 140 MeV have a larger χ^2/F than the other cases. Nevertheless, the results listed in table 7 follow all the trends found

TABLE 5
Parameters of the real folded and the imaginary potentials for elastic α-particle scattering at 172.5 MeV

Target	^{58}Ni			^{60}Ni			^{62}Ni			^{64}Ni		
Absorption	WS	$(WS)^2$	$(WS)^2+D$	WS	$(WS)^2$	$(WS)^2+D$	WS	$(WS)^2$	$(WS)^2+D$	WS	$(WS)^2$	$(WS)^2+D$
λ	1.374	1.316	1.325	1.344	1.326	1.334	1.346	1.321	1.332	1.341	1.317	1.330
λU_F (MeV)	142.1	136.0	137.0	138.5	136.6	137.5	138.5	135.9	137.1	138.3	135.8	137.2
W_V (MeV)	17.74	31.71	31.65	25.72	26.77	28.94	23.58	26.03	34.87	20.80	24.49	41.57
r_V (fm)	1.604	1.571	1.480	1.406	1.659	1.520	1.467	1.675	1.326	1.529	1.698	1.156
a_V (fm)	0.663	1.437	1.536	0.912	1.288	1.486	0.848	1.249	1.717	0.789	1.232	1.934
W_D (MeV)			2.224			2.686			5.002			6.284
r_D (fm)			1.594			1.592			1.562			1.546
a_D (fm)			0.849			0.856			0.946			0.982
J_U (MeV · fm^3)	270.2	258.7 (257.8)	260.7	267.0	263.4 (267.7)	265.0	269.0	264.0 (264.7)	266.3	268.8	264.0 (266.9)	266.6
$\langle r_U^2\rangle^{1/2}$ (fm)	4.578	4.578 (4.603)	4.578	4.642	4.642 (4.689)	4.642	4.698	4.698 (4.710)	4.698	4.743	4.743 (4.768)	4.743
J_W (MeV · fm^3)	85.14	91.95 (89.18)	89.56	95.10	91.65 (91.04)	90.80	94.17	92.11 (92.76)	91.84	90.61	90.63 (91.21)	91.11
$\langle r_W^2\rangle^{1/2}$ (fm)	5.402	5.280 (5.201)	5.312	5.447	5.363 (5.301)	5.394	5.489	5.410 (5.297)	5.464	5.572	5.497 (5.404)	5.565
χ^2/F	11.16	3.78 (4.92)	2.04	6.57	3.89 (2.83)	2.43 [a])	10.80	8.83 (4.65)	7.28 [a])	6.07	4.50 (1.70)	2.57

Numbers in parentheses refer to real and imaginary potentials in the $(WS)^2$ form.
[a]) See text of sect. 6 for comment.

TABLE 6

Parameters of the real folded and the imaginary potentials for elastic α-particle scattering at 140 MeV

Target	^{40}Ca			^{58}Ni			^{90}Zr			^{208}Pb		
Absorption	WS	$(WS)^2$	$(WS)^2+D$	WS	$(WS)^2$	$(WS)^2+D$	WS	$(WS)^2$	$(WS)^2+D$	WS	$(WS)^2$	$(WS)^2+D$
λ	1.338	1.318	1.305±0.016	1.311	1.293	1.297	1.324	1.310	1.302	1.380	1.355	1.363
λU_F (MeV)	142.2	140.1	138.7±1.7	147.8	145.8	146.2	151.5	149.9	149.0	155.3	152.5	153.4
W_V (MeV)	19.18	21.84	23.93±1.91	20.91	23.07	30.88	19.20	22.42	19.45	19.15	21.23	20.43
r_V (fm)	1.597	1.788	1.694±0.011	1.500	1.703	1.252	1.538	1.678	1.713	1.512	1.618	1.613
a_V (fm)	0.701	1.078	1.192±0.073	0.794	1.146	1.572	0.719	1.107	1.051	0.637	0.989	0.856
W_D (MeV)			1.057±0.760			6.537			3.446			0.336
r_D (fm)			1.826±0.061			1.524			0.865			1.810
a_D (fm)			0.685±0.22			1.065			1.153			0.614
J_U (MeV·fm^3)	296.0	291.7	288.8±4.6	277.7	273.9	274.7	281.3	278.3	276.8	288.4	283.2	284.9
$\langle r_U \rangle$ (fm)	4.288	4.288	4.288	4.558	4.558	4.558	5.079	5.079	5.079	6.292	6.292	6.292
J_W (MeV·fm^3)	95.05	94.55	94.34	87.43	86.4	86.46	80.91	82.09	82.27	72.69	73.76	73.34
$\langle r_W \rangle$ (fm)	4.969	4.920	4.928	5.379	5.290	5.297	5.970	5.872	5.845	7.332	7.253	7.259
χ^2/F	10.16	3.54	1.01	4.33	2.05	1.81	9.00	2.71	1.87	8.31	6.91	5.42

TABLE 7

Parameters of the real folded and the imaginary potentials for elastic α-particle scattering at 140 MeV from Ti isotopes

Target	^{46}Ti			^{48}Ti			^{50}Ti		
Absorption	WS	$(WS)^2$	$(WS)^2+D$	WS	$(WS)^2$	$(WS)^2+D$	WS	$(WS)^2$	$(WS)^2+D$
λ	1.304	1.272	1.282	1.307	1.282	1.300	1.332	1.311	1.314
λU_F (MeV)	141.9	138.3	139.5	142.4	139.7	141.6	145.9	143.6	143.9
W_V (MeV)	21.64	26.82	25.04	19.31	22.65	31.07	16.99	20.42	32.57
r_V (fm)	1.571	1.723	1.725	1.608	1.769	1.364	1.637	1.776	1.201
a_V (fm)	0.742	1.220	1.228	0.683	1.090	1.589	0.638	1.041	1.564
W_D (MeV)			1.139			5.598			6.882
r_D (fm)			1.716			1.614			1.592
a_D (fm)			0.408			0.890			0.949
J_{tr} (MeV · fm^3)	287.3	280.1	282.3	286.7	281.2	285.0	290.0	285.3	286.0
$\langle r_U^2\rangle^{1/2}$ (fm)	4.432	4.432	4.432	4.461'	4.461	4.461	4.482	4.482	4.482
J_W (MeV · fm^3)	102.8	102.9	100.7	95.26	95.40	95.91	86.54	87.68	88.17
$\langle r_W^2\rangle^{1/2}$ (fm)	5.160	5.095	5.143	5.189	5.135	5.186	5.238	5.169	5.171
χ^2/F	18.80	13.84	7.26	25.16	20.05	12.97 [a])	14.79	9.60	4.66

[a]) See text of sect. 6 for comment.

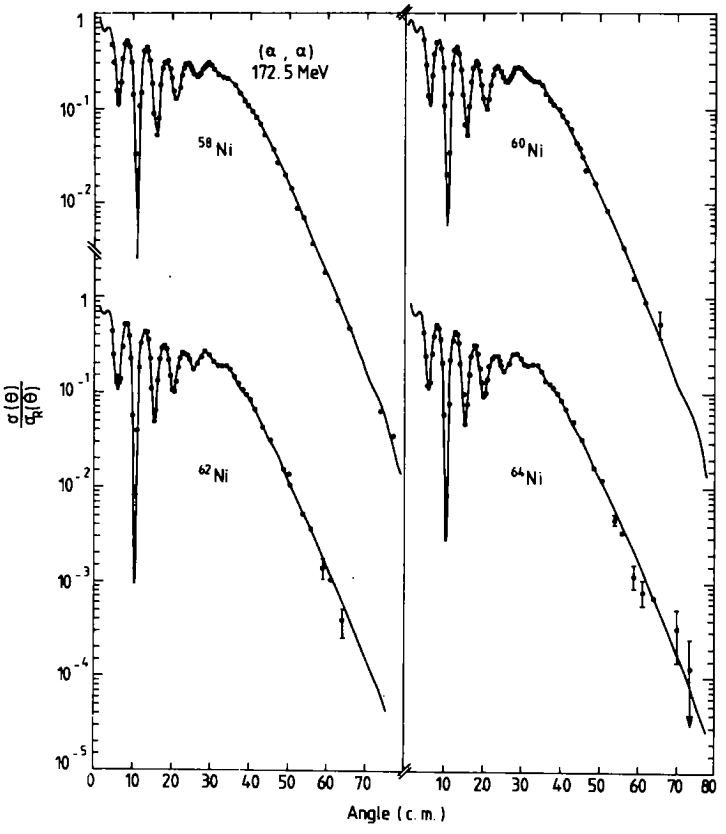

Fig. 2. The fits to 172.5 MeV α-particle elastic scattering from ^{58,60,62,64}Ni isotopes calculated with the density-dependent M3Y folded real and volume+derivative Woods–Saxon-squared imaginary potentials.

for the remaining targets and thus constitute additional support for our model. In particular, the renormalizing factor λ for the Ti isotopes is very close to that for other targets, and so are the features of the imaginary potentials (discussed below).

The best fit is obtained for ^{50}Ti which has closed neutron shells. We note that the calculated densities may not be as good in the case of non-closed shells for protons and neutrons in ^{46}Ti and ^{48}Ti. We also comment that for ^{48}Ti a very large fraction of χ^2/F comes from the far rainbow region where the experimental data [14]) have some unusual wiggling.

We now discuss our results concerning the potentials and densities.

6.1. THE REAL POTENTIAL

In fig. 3 we show different real potentials for ^{58}Ni(α, α) at 172.5 MeV together with the imaginary potential accompanying the "best fit" DDM3Y real potential.

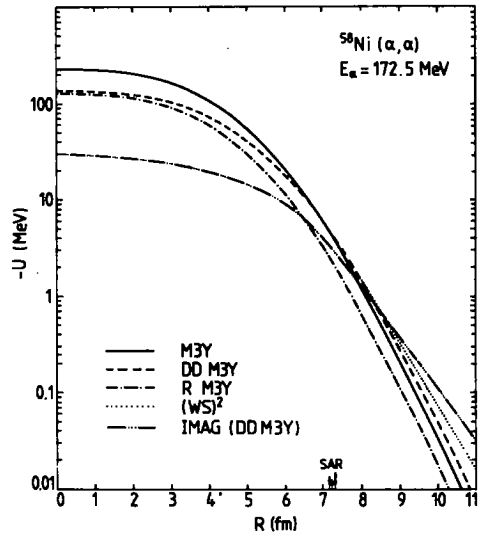

Fig. 3. The real potentials calculated with different approaches to the M3Y folding model and the imaginary potential for ^{58}Ni(α, α) scattering at 172.5 MeV, as discussed in text.

This graph and table 5 enables us to draw some conclusions about the real potential:

(i) The central depth of the real potential that can fit the data well in the whole angular region is very well established (to within less than 2%) in accordance with phenomenological analyses [4]). The normalizing factor λ changes very little with the mass number and energy.

(ii) The unnormalized M3Y real potential is much deeper in the centre than the density dependent M3Y (DDM3Y) potential but it is quite close to the latter in the nuclear surface, at the strong absorption radius (SAR), and that is why it can fit well the forward angle data, but cannot fit the rainbow cross section, as mentioned in subsect. 3.1. The inner part of the potential affects the large angle scattering.

(iii) The phenomenological (WS)^2 real potential is very close to the DDM3Y up to about 9 fm and its volume integral and rms radius are very similar to those of the latter.

(iv) The volume integrals of the real potentials change little with A, slightly decreasing with A, in accord with other predictions involving density dependence [39]). The volume integrals are smaller and vary less with A than those reported from a model-independent analysis [38]). In accord with ref. [38]), for a single case of ^{58}Ni, we found them to decrease with energy at the rate 0.45 MeV · fm^3/MeV, in the energy range 140–173 MeV.

6.2. THE IMAGINARY POTENTIALS

In all cases we found a definite superiority of the Woods–Saxon squared imaginary volume potential over the Woods–Saxon one. Moreover, having achieved very good fits with the $(WS)^2$ imaginary volume potential, we were tempted to allow the imaginary potential a greater flexibility in shape, adding a derivative of the $(WS)^2$ term with its geometry independent of that of the volume term. Unexpectedly, with a weak derivative term we found a statistically meaningful improvement in the fits with the reduction of χ^2/F often by a factor of 2.

A similar parametrization was successfully used by Budzanowski *et al.* [40]) who found evidence for a weak surface form with rather similar parameters for ^{58}Ni(α, α) at 139 MeV [ref. [12])] analysed with Woods–Saxon-squared real and imaginary potentials.

The volume integrals and rms radii of the imaginary potentials are very similar for the two cases involving the $(WS)^2$ form factor. Thus it seems that the bulk characteristics of the imaginary potential are very well determined once the fits become very good.

We did not see any instability of the volume integrals of the real potential nor a coupling of the imaginary potential to the real one when using a $(WS)^2$ form factor, as has been reported elsewhere [38]). Our rms radii of the imaginary potential are slightly larger than those of ref. [38]); however in agreement with this reference we found that the volume integral of the imaginary potential decreased with mass number and increased with energy.

Our findings about the shape of the imaginary potential cast some doubt on phenomenological claims [14,38,39]) that the imaginary optical potential for α-particles should be exclusively of a Woods–Saxon shape. It could even be worthwhile to revive the problem of a model-independent imaginary potential, since it is the imaginary potential that is particularly liable to mock up the contributions from higher order processes.

We note that in each case under study, no matter what starting parameter values were chosen, the sequence of MINUIT [10]) searches converged to extremely similar final parameters.

For one case, ^{40}Ca(α, α) at 141.7 MeV where we have reached the statistically meaningful limit of $\chi^2/F = 1$ we give in table 6 the uncertainties of the final potential parameters as calculated by MINUIT from the inverted covariance matrix. These uncertainties are quite small and they mean that within their limits there exists another set of parameters that could produce a fit with a χ^2/F changed by 1. There is, obviously, no free choice of the parameters within those limits since the parameters, peculiarly those of the imaginary potential, are strongly correlated. However, the normalization λ is fixed very precisely and it is very weakly correlated with the imaginary potential.

We mention here that we also tried to fit ^{58}Ni(α, α) scattering at 172.5 MeV with both the real and imaginary potentials derived from the DDM3Y, i.e. taking

the imaginary potential to have the same shape as the real one derived from the DDM3Y, i.e. the λ normalizing factor being complex. This resulted in $\lambda = 1.387 + 0.672i$ and $\chi^2/F = 53$. The fit was particularly bad in the region of the rainbow angle. A similar feature was also found in an earlier study [41]). In a search restricted to forward angles only ($\theta < 30°$) λ was $1.414 + 0.727i$ and $\chi^2/F = 45$. These results mean that the imaginary potential definitely requires a different shape from the real potential.

In table 8 we list for some cases the strong absorption radius, SAR, defined as [3])

$$\mathrm{SAR} = \frac{1}{k}[n + (n^2 + L_{1/2}^2)^{1/2}], \tag{17}$$

where $L_{1/2}$ is the (interpolated) angular momentum for which the transmission coefficient $T_{L_{1/2}} = 1 - |S_{L_{1/2}}|^2 = 0.5$, k is the wavenumber and n is the Sommerfeld parameter. Also listed are the real potentials at this radius, U(SAR). In addition we give the ratio of the imaginary $(\mathrm{WS})^2$ potential to the real double-folded potential (W/U) at this radius, and α, the inverse of the logarithmic derivative of the real potential at SAR, as the measure of the slope of the real potential.

TABLE 8

Characteristics of the potentials at the strong absorption radius (SAR)

Potential	SAR (fm)	$-U$(SAR) (MeV)	W/U	$-\alpha$	χ^2/F	Reaction
DDM3Y	7.26	4.28	0.69	0.75	2.05	^{58}Ni(α, α) at 172.5 MeV
M3Y	7.22	4.04	0.74	0.69	5×10^5	
RM3Y	7.29	2.04	1.36	0.63	89	
M3YF	7.27	3.62	0.78	0.65	3.00	
RDDD	7.59	1.08	3.08	0.61	98	
$(\mathrm{WS})^2$	7.17	4.60	0.67	0.77	4.51	
DDM3Y	7.31	4.11	0.67	0.78	1.81	^{58}Ni(α, α) 140 MeV
DDM3Y	6.72	4.54	0.66	0.77	1.01	^{40}Ca(α, α) 140 MeV

DDM3Y: Density dependent M3Y potential as used in this paper.
M3Y: Pure M3Y potential.
RM3Y: Renormalized M3Y potential so as to roughly fit the data for all angles.
M3YF: Renormalized M3Y potential so as to fit the data for forward angles.
RDDD: Renormalized density-dependent potential with the DDD density-dependent interaction.
$(\mathrm{WS})^2$: Woods–Saxon squared potential.
The imaginary potentials are the $(\mathrm{WS})^2$ [eq. (2b)] except for the DDM3Y entries where these are the $(\mathrm{WS})^2 + \mathrm{D}$ [eq. (2c)].

It is clear from table 8 that to fit the data, even at forward angles only, the W/U at the SAR must be less than 1. The heavily renormalized M3Y and DDD potentials that failed to fit the data lack this property. For other targets the ratio W/U was very similar to the value listed for ^{58}Ni and ^{40}Ca. We also see from fig. 3 that while

the imaginary potential is appreciably weaker than the real one in the interior region, it becomes stronger at radii about 2 fm beyond the SAR.

6.3. THE NUCLEAR MATTER DENSITIES

Our previous knowledge of the proton and neutron densities in ^{40}Ca is rather complete because model-independent charge distributions have been extracted from elastic electron scattering data [42]) and because the difference between the proton and neutron distributions can be calculated relatively accurately since it is due to the Coulomb force. Thus as we have argued previously [43,44]), ^{40}Ca should be used primarily as a test for the reaction theory models and to test their sensitivity to the neutron distribution.

The entries in the row labelled "best" in table 9 are based on the experimental charge density, which we have characterized by the two moments $r_{ch} = \langle r^2 \rangle_{ch}^{1/2}$ and $\langle r^4 \rangle_{ch}^{1/4}$ [or equivalently r_{ch} and $\tilde{a}_{ch}$ via eq. (13)] and the density of nucleon charge near the centre $\rho_{ch}(r = 0)$. The quantities $r_n - r_p$ and $\tilde{a}_n - \tilde{a}_p$ (which refer to the point nucleon densities) for the "best" parameters came from the Hartree–Fock calculation which takes into account the self-consistency between the Coulomb and isovector nuclear potentials [43]). Actually, none of the individual calculations which we have made are able to reproduce all of these "best" parameters. In particular the defects with the Woods–Saxon are that $r_n - r_p$ is too large because the self-consistency between the Coulomb and isovector nuclear potentials is not taken into account and that the density at the origin is too large, whereas the defect in the Skyrme Hartree–Fock results is that the diffuseness $\tilde{a}$ is too small.

The α-scattering data are insensitive to the interior density and we will therefore confine our remarks to the sensitivities to $r_n - r_p$ and the diffuseness $\tilde{a}$. It is a good approximation to correct the Woods–Saxon $r_n - r_p$ defect by making a radial

TABLE 9

^{40}Ca density parameters

	r_{ch} (fm)	$\tilde{a}_{ch}$ (fm)	$r_n - r_p$ (fm)	$\tilde{a}_n - \tilde{a}_p$ (fm)	$\rho_{ch}(r=0)$ (nucleons/fm^3)	χ^2/F [d])
"best" [a])	3.483	0.520	−0.036	−0.014	0.088	
WS−2 [b])	3.483	0.522	−0.154	−0.034	0.097	3.6
WS+0	3.483	0.522	−0.089	−0.024	0.097	1.2
WS+2	3.483	0.522	−0.023	−0.016	0.097	1.6
WS+5	3.483	0.522	0.076	−0.010	0.097	8.4
HF [c])	3.483	0.476	−0.036	−0.014	0.082	1.0

[a]) See text of subsect. 6.3.

[b]) $\pm N$ refers to results with a neutron density rescaled to give a neutron rms radius which is $\pm N$% different from the original Woods–Saxon calculation.

[c]) Hartree–Fock calculation with a Skyrme 3 interaction.

[d]) χ^2 per degree of freedom.

adjustment of the neutron density with the monopole Werntz and Überall model [33]) [eq. (16)]. We have varied the neutron radius by ±2% and ±5% and in each case have fit the alpha scattering data by allowing the imaginary potential and overall normalization to vary and the results for the χ^2 per degree of freedom, χ^2/F, are given in table 9.

By taking the limits where χ^2/F increases by a factor of two to determine the error we obtain $r_n - r_p = -0.07 \pm 0.06$ fm. This error could only be reduced by making some further theoretical assumptions about the imaginary potential or about the overall normalization. An error of ±0.06 fm is encouraging in that it is about the same as obtained from high energy proton scattering. [Errors quoted for the matter radii $r_m \approx \frac{1}{2}(r_n + r_p)$ from high energy proton scattering are typically as small as ±0.03 fm [ref. [44])] which gives a ±0.06 fm error for $r_n - r_p$ since $r_n - r_p \approx 2(r_m - r_p)$ and r_p is accurately known from the charge radius.] However, an error of ±0.06 fm is rather large relative to the variations between different reliable theoretical predictions for the quantity $r_n - r_p$ which are typically less than ±0.03 fm.

By comparing the "WS+2" and "HF" results in table 9 we can conclude that if $r_n - r_p$ is fixed then the matter diffuseness $\tilde{a}_m$ can be extracted from analyses of α-particle elastic scattering with an error of about ±0.09 fm.

The next stage would be to somehow vary both $r_n - r_p$ and the diffuseness. However, it is clear in this case that the error in both will be larger than before. The logical continuation of this process of increasing the number of parameters is the "model-independent" density as used for example by the Karlsruhe group [39]) for which the error band and error in $r_n - r_p$ would probably be too large for a meaningful comparison with theory.

At present the errors on the determined densities can only be kept reasonably small by limiting the family of shapes to those which are theoretically reasonable as obtained from Woods–Saxon and Hartree–Fock bound-state potential models as we have done in this work.

Since χ^2/F is near unity for the values of $r_n - r_p$ and $\tilde{a}_{ch}$ which are near the "best" values in ^{40}Ca, we conclude that the folding model approach is successful for ^{40}Ca and that various nuclear matter distributions for other nuclei can be tested in the sense that a small χ^2/F indicates a "consistent" neutron and proton density, since it is improbable that errors in both the folded potentials and the densities would cancel to give a small χ^2/F.

However, if χ^2/F is much larger than unity for some other nuclei it is in general not possible to ascribe this to a fault in only the folded potential description or a fault in only the calculated density. The above remarks pertain to absolute cross sections and densities; it would be interesting in the future to investigate the uncertainties in our approach to a folding model analysis of relative cross sections and densities such as in an isotopic sequence.

The Ni densities calculated with the configuration mixed occupation numbers of Koops [26]) differ from the densities calculated with the extreme single-particle

occupation numbers primarily in the matter diffuseness parameter which is 0.005 to 0.020 fm larger in the former case (see table 4). The results for the α-scattering fits with the mixed configuration densities (see tables 5 and 6) give χ^2/F values between 2 and 3 for the Ni isotopes which are somewhat worse than for ^{40}Ca. It is encouraging that the less reliable densities obtained with the extreme single-particle occupation numbers give about a 50% larger χ^2/F for the Ni isotopes. With $r_n - r_p$ fixed, a change in $\tilde{a}_m$ of about ± 0.04 fm has resulted in an increase in χ^2/F by a factor of two.

7. Conclusions and discussion

Using a generalization of the M3Y interaction which incorporates a density dependence based upon nuclear matter calculations we fitted very well the differential cross sections for the elastic scattering of α-particles by nuclei of different mass numbers at two energies 140 and 173 MeV, where the rainbow scattering was observed. We proved that this interaction can work well and consistently, enabling a precise determination of the depth of the folded potential. However, the folded density-dependent M3Y potential has to be renormalized by the considerable but almost universal factor of 1.3. The proposed density dependence appeared to be too strong. Although we note that the results of ref. [23]) show that if we had chosen the density ρ in eq. (7) to be that midway between the two nucleons, the renormalization required would be some 10% smaller.

One possible reason for needing $\lambda > 1$ is that the G-matrix upon which our interaction is based is for a single nucleon traversing nuclear matter. However, we are concerned here with two pieces of nuclear matter moving relative to one another and not being simply superimposed. In this situation the effect of the Pauli principle may be weakened and the effective interaction be somewhat stronger than the one we have used. There are also indications that the shape of the effective interaction may depend on the density [45]). A recent, more accurate approach to the density and energy dependence in the effective interaction by Faessler *et al.* [46]) does take these effects into account. It however also assumes no readjustment of the densities in the region where they overlap.

Nevertheless, the model we have been using does work rather well and consistently over a range of nuclei and we can regard it as a semi-phenomenological density-dependent M3Y folding model.

We note that the alternative prescription of taking the density of the system as the geometrical mean of the two densities as used in a single-folding model [47]) avoids the build up of high densities but it weakens the density dependence in the important region where two low densities overlap. However, this prescription considerably overestimates the depth of the real potential and a renormalizing factor of 0.6–0.7 was required to get good fits.

We found a definite preference for the imaginary potential to have the Woods–Saxon-squared form supplemented by a weak surface term. Much worse fits were obtained with the Woods–Saxon form factor of the imaginary potential.

We find in general that uncertainties in the folding model real and imaginary potential parameters can be partially mocked up by uncertainties in the nuclear densities distributions even when the fits to data are very good. The "model-independent" density extracted from a fit to experiment will have an error band which is too large to make comparison with theoretical densities meaningful. Hence our strategy has been to start with densities which have a very restricted family of shapes based on single-particle potential models which already reproduce as well as possible the experimental charge distribution.

^{40}Ca can be used mainly as a test of the scattering potential model since the density shape is already well determined and we find that the folding model theory with a reasonable renormalization works remarkably well. From the fits to ^{40}Ca data, the sensitivity to $r_n - r_p$ is ± 0.06 fm and the sensitivity to the diffuseness $\tilde{a}$ is about ± 0.09 fm (taking into account no correlation between these two parameters), which are about the same size as has been previously extracted from high energy proton scattering [43,44]) but are still rather large to be a very sensitive test of the currently most reliable theoretical models.

A.M.K. thanks Dr J.R. Rook for discussions and Dr J. Cook for permission to modify and use his folding code. A.M.K. is also grateful to Professor P.J. Wurm for hospitality in Heidelberg and to Max Planck Institute fur Kernphysik, Heidelberg – where this work was started – for support, and to the British Council and the Science and Engineering Research Council for enabling a stay at Nuclear Physics Laboratory, Oxford, where it was finished.

References

1) D.A. Goldberg, Phys. Lett. **55B** (1975) 59
2) D.M. Brink and N. Takigawa, Nucl. Phys. **A279** (1977) 159
3) G.R. Satchler and W.G. Love, Phys. Reports **55** (1979) 183
4) D.A. Goldberg, Proc. 2nd Louvain-Cracow Seminar on the Alpha-nucleus interaction, 1978, ed. G. Gregoire and K. Grotowski (Louvain University, 1978) p. 41
5) Z. Majka, H.G. Gils and H. Rebel, Z. Phys. **A288** (1978) 139
6) Y. Eisen and B. Day, Phys. Lett. **63B** (1976) 253
7) C. B. Dover and J.P. Vary, Phys. Rev. Lett. **31** (1973) 1510
8) N. Vinh Mau, Phys. Lett. **71B** (1977) 5
9) J. Cook, King's College London Report, unpublished (1980)
10) F. James and M. Roos, Comp. Phys. Comm. **10** (1975) 343
11) A. Budzanowski, C. Alderliesten, J. Bojowald, W. Oelert, P. Turek, H. Dabrowski and S. Wiktor, Proc. Int. Discussion Meeting on What do we know about radial shape of nuclei in the Ca region?, Karlsruhe, 1979, ed. H. Rebel, H.J. Gils and G. Shatz (Kernforschunszentrum Karlsruhe, 1979) p. 377
12) D.A. Goldberg, S.M. Smith and G.F. Burdzik, Phys. Rev. **C10** (1974) 1362

13) D.A. Goldberg, S.M. Smith, H.G. Pugh, P.G. Roos and N.S. Wall, Phys. Rev. **C7** (1973) 1938
14) P.L. Roberson, D.A. Goldberg, N.S. Wall, L.W. Woo and H.L. Chen, Phys. Rev. Lett. **42** (1979) 54
15) G. Bertsch, J. Borysowicz, H. McManus and W.G. Love, Nucl. Phys. **A284** (1977) 399
16) J. Cook and R.J. Griffiths, Nucl. Phys. **A366** (1981) 27
17) W. G. Love, Phys. Rev. **C17** (1978) 1876
18) R. Ceuleneer, Proc. 2nd Louvain-Cracow Seminar on the Alpha-nucleus interaction, 1978, ed. G. Gregoire and K. Grotowski (Louvain University, 1978) p. 185
19) F. Petrovich, D. Stanley and J. J. Bevelcqua, Phys. Lett. **71B** (1977) 259
20) J.P. Jeukenne, A. Leujenne and C. Mahaux, Phys. Rev. **C16** (1977) 80
21) W.D. Myers, Nucl. Phys. **A204** (1973) 465
22) W.G. Love, Phys. Lett. **72B** (1977) 4
23) L.J.B. Goldfarb and P. Nagel, Nucl. Phys. **A341** (1980) 494
24) G.R. Satchler, 1980 (unpublished)
25) J.R. Durell, C.A. Harter, J.M. Mo and W.R. Phillips, Nucl. Phys. **A334** (1980) 144; M.A. Franey, J.S. Lilley and W.R. Phillips, Nucl. Phys. **A324** (1979) 193
26) J.E. Koops and P.W.M. Glaudemans, Z. Phys. **A280** (1977) 181
27) D. Vautherin and D.M. Brink, Phys. Rev. **C5** (1972) 626
28) M. Beiner, H. Flocard, N. Van Giai and P. Quentin, Nucl. Phys. **A238** (1975) 29
29) H.D. Wohlfahrt, E.B. Shera, M.V. Hoehn, Y. Yamazaki and R.M. Steffen, Phys. Rev. **C23** (1981) 533
30) H.D. Wohlfahrt, O. Schwentker, G. Fricke, H.G. Andresen and E.B. Shera, Phys. Rev. **C22** (1980) 264
31) H. Rothaas, dissertation thesis, Mainz, unpublished (1976)
32) B. Frois, J.B. Bellicard, J.M. Cavedon, M. Huet, P. Leconte, P. Ludeau, A. Nakad, P.Z. Ho and I. Sick, Phys. Rev. Lett. **38** (1977) 152
33) C. Werntz and H. Überall, Phys. Rev. **149** (1966) 762
34) I. Sick, private communication (1979)
35) R.G. Arnold, B.T. Chertok, S. Rock, W.P. Schutz, Z.M. Szalata, D. Day, J.S. McCarthy, F. Martin, B.A. Mecking, I. Sick and G. Tamas, Phys. Rev. Lett. **40** (1978) 1429
36) J.S. McCarthy, I. Sick and R.R. Whitney, Phys. Rev. **C15** (1977) 1396
37) J. Borysowicz and D.O. Riska, Nucl. Phys. **A254** (1975) 301
38) E. Friedman, H.J. Gils, H. Rebel and R. Pesl, Nucl. Phys. **A363** (1981) 137
39) H.J. Gils, E. Friedman, Z. Majka and H. Rebel, Phys. Rev. **C21** (1980) 1245
40) A. Budzanowski, H. Dabrowski, L. Freindl, K, Grotowski, S. Micek, R. Planeta, A. Strzalkowski, M. Bosman, P. Leleux, P. Macq, J.P. Meulders and C. Pirart, Phys. Rev. **C17** (1978) 951
41) C.B. Dover, J.P. Vary, Proc. Symp. on classical and quantum mechanical aspects of heavy-ion collisions, Heidelberg 1974 (Springer, Berlin, 1975)
42) I. Sick, J.B. Bellicard, J.M. Cavedon, B. Frois, M. Huet, P. Leconte, P.X. Ho and S. Platchkov, Phys. Lett. **88B** (1979) 245
43) B.A. Brown, S.E. Massen and P.E. Hodgson, J. of Phys. **G5** (1979) 1655
44) B.A. Brown, S.E. Massen and P.E. Hodgson, Proc. Int. Discussion Meeting on What do we know about radial shape of nuclei in the Ca region?, Karlsruhe, 1979, ed. H. Rebel, H.J. Gils and G. Shatz (Kernforschungszentrum Karlsruhe, 1979) p. 377
45) F.A. Brieva, H.V. Geramb and J.R. Rook, Phys. Lett. **79B** (1978) 177
46) A. Faessler, T. Izumoto, S. Krewald and R. Sartor, Nucl. Phys. **A359** (1981) 509
47) F. Duggan, M. Lassaut, F. Michel and N. Vinh Mau, Nucl. Phys. **A355** (1981) 141